NANO · MICRO small
www.small-journal.com

Sustainable Production of Biomass-Derived Graphite and Graphene Conductive Inks from Biochar

Haoyang You, Janan Hui, Yilun Zhou, Kayla Vittore, Jinrui Zhang, Lindsay E. Chaney, Sritarun Chinta, Yunhao Zhao, Gilhwan Lim, DoKyoung Lee, Elizabeth A. Ainsworth, Jennifer B. Dunn, Vinayak P. Dravid, Mark C. Hersam, and Stuart J. Rowan**

Graphite is a commonly used raw material across many industries and the demand for high-quality graphite has been increasing in recent years, especially as a primary component for lithium-ion batteries. However, graphite production is currently limited by production shortages, uneven geographical distribution, and significant environmental impacts incurred from conventional processing. Here, an efficient method of synthesizing biomass-derived graphite from biochar is presented as a sustainable alternative to natural and synthetic graphite. The resulting bio-graphite equals or exceeds quantitative quality metrics of spheroidized natural graphite, achieving a Raman I_D/I_G ratio of 0.051 and crystallite size parallel to the graphene layers (L_a) of 2.08 µm. This bio-graphite is directly applied as a raw input to liquid-phase exfoliation of graphene for the scalable production of conductive inks. The spin-coated films from the bio-graphene ink exhibit the highest conductivity among all biomass-derived graphene or carbon materials, reaching $3.58 \pm 0.16 \times 10^4$ S m^{-1}. Life cycle assessment demonstrates that this bio-graphite requires less fossil fuel and produces reduced greenhouse gas emissions compared to incumbent methods for natural, synthesized, and other bio-derived graphitic materials. This work thus offers a sustainable, locally adaptable solution for producing state-of-the-art graphite that is suitable for bio-graphene and other high-value products.

1. Introduction

Graphite, a crystalline allotrope of carbon, is a crucial material with diverse applications ranging from lubrication in metal processing to the production of essential components for electronics and energy storage.[1,2] In particular, rising demand for graphite in lithium-ion batteries has led to a global shortage,[3,4] prompting countries, such as the United States,[5] European Union,[6] and Australia,[7] to identify it as a critical mineral or material. Furthermore, material flow analyses of graphite for the United States highlight the vulnerability of supply chains due to reliance on imported graphite.[8] These concerns are exacerbated as China, the world's largest graphite exporter, continues to tighten its controls on graphite exports in recent years.[9] Graphite can be classified as natural or synthetic based on its sourcing and processing. Natural graphite from mining is more achievable in bulk and is commonly used for

H. You, S. J. Rowan
Department of Chemistry
University of Chicago
5735 S Ellis Ave, Chicago, IL 60637, USA
E-mail: stuartrowan@uchicago.edu
J. Hui, M. C. Hersam
Department of Chemistry
Northwestern University
2145 Sheridan Rd, Evanston, IL 60208, USA
E-mail: m-hersam@northwestern.edu
Y. Zhou, J. Zhang, J. B. Dunn
Department of Chemical and Biological Engineering
Northwestern University
2145 Sheridan Road, Evanston, IL 60208, USA
The ORCID identification number(s) for the author(s) of this article can be found under https://doi.org/10.1002/smll.202406669

DOI: 10.1002/smll.202406669

K. Vittore, D. Lee
Department of Crop Sciences
University of Illinois Urbana-Champaign
1102 S Goodwin Ave, Urbana, IL 61801, USA
L. E. Chaney, S. Chinta, G. Lim, V. P. Dravid, M. C. Hersam
Department of Materials Science and Engineering
Northwestern University
2220 Campus Drive, Evanston, IL 60208, USA
Y. Zhao, S. J. Rowan
Pritzker School of Molecular Engineering
The University of Chicago
5640 S Ellis Ave, Chicago, IL 60637, USA
G. Lim, V. P. Dravid
The NUANCE Center
Northwestern University Evanston
2145 Sheridan Rd, Evanston, IL 60208, USA
E. A. Ainsworth
USDA-ARS
Global Change and Photosynthesis Research Unit
1201 W. Gregory Drive, Urbana, IL 61801, USA
M. C. Hersam
Department of Electrical and Computer Engineering
Northwestern University
2145 Sheridan Rd, Evanston, IL 60208, USA

refractory and lubricant applications. On the other hand, synthetic graphite is characterized by smaller crystallite sizes and enhanced purity that is important for higher-value products such as coatings and conductive fillers.[2,10] The production of both natural and synthetic graphite has significant environmental drawbacks. Mining natural graphite causes land disturbance and produces substantial dust emissions through multiple stages of attrition milling and flotation, and downstream purification of natural graphite requires the large-scale use of energy and harmful agents, such as hydrofluoric acid leaching, halogen or alkali roasting, and thermal treatment in inert atmospheres.[11] Synthetic graphite, typically produced from fossil fuels, particularly petroleum needle coke and coal tar pitch, involves multiple energy-intensive heating processes. Specifically, residue from vacuum-distilled petroleum oil and coal tar pitch are calcinated and baked at 800-1000 °C before then undergoing graphitization at ≈3000 °C.[11] Overall, substantial environmental and economic concerns exist for the production of both types of graphite, thus motivating the identification of sustainable alternatives.

Recently, research on bio-graphite production from raw biomass has gained traction, utilizing transition metals such as iron, cobalt, and nickel as catalysts to facilitate graphitization at temperatures below 2000 °C.[12] Among these metals, iron is the most common catalyst due to its high catalytic activity and abundance in nature.[12] In iron-based catalysis of graphitization, carbon undergoes a dissolution-precipitation mechanism at temperatures exceeding 750 °C, where amorphous carbon from biomass is dissolved into the iron bulk, and subsequently, graphene layers precipitate on the iron surface to form graphitic structures.[13,14] For example, Yan et al. used iron nitrate to catalyze the graphitization of kraft lignin at 1000 °C under different gas atmospheres. This process produces graphene-encapsulated iron nanoparticles where the size of the graphene shells can range from a few nanometers to 20 nm.[15] In another case, Banek et al. prepared Li-ion battery-grade bio-based "potato-shaped" graphite by employing laser beam heating on biochar and metal catalysts.[16,17] Despite the efficiency of laser beam heating in terms of time and energy, the process involved heating to temperatures up to 1580 °C, followed by rapid cooling.[17] Likewise, Sagues et al. used iron powder to catalyze the conversion of various biomaterials to crystalline graphite at 1200 °C, where their bio-graphite only reached crystal size up to 30 nm despite reasonable performance in lithium-ion battery anodes.[18] Overall, graphite production from biomass waste materials have shown limited graphitic structure based on Raman spectroscopy and X-ray diffraction (XRD) measurements, suggesting the presence of turbostratic or disordered carbon after graphitization, which limits applicability toward high-value products such as few-layer graphene.[19]

In this study, a method is developed to sustainably produce bio-graphite derived from hardwood biochar which can be alternatively sourced from the cellulosic renewable diesel industry. The approach involves a sequence of steps: pre-heating carbonization of biomass, iron-catalyzed graphitization, and iron removal with acid. A systematic investigation was conducted to understand the effects of both the iron catalyst loading and heating procedure on the final product. Optimization of these parameters resulted in a procedure that yields bio-graphite with a crystallite size comparable to commercial spheroidized natural graphite, representing the largest value for biomass-derived graphite reported to date. The large graphite crystallite size enables the production of high-conductivity graphene inks. In particular, the bio-graphite is used in liquid-phase exfoliation to create bio-graphene nanoplatelets for printable and spin-coatable conductive inks that are suitable for additive manufacturing of electronic device components. Spin-coated films of the bio-graphene ink exhibit the highest conductivity among printable biomass-derived graphene materials, reaching $3.58 \pm 0.16 \times 10^4$ S m^{-1}. This conductivity is comparable to graphene inks made from natural graphite, highlighting the application of bio-graphite toward higher value products. Life cycle assessment (LCA) of this process demonstrates lower fossil fuel demand and greenhouse gas (GHG) emissions compared to traditional graphite production methods. By leveraging agricultural residues and other excess biomass, this approach can enable local graphite production to reduce transportation costs and minimize emissions, making it an eco-friendly alternative to combat the rising global demand for high-quality graphite and graphene.

2. Results and Discussion

2.1. Optimization of Bio-Graphite Synthesis

The bio-graphite preparation process is outlined in the flowchart presented in **Figure 1**. The synthesis involves four key steps: pre-heating carbonization of the biomass to yield biochar and bio-oil, mixing biochar and iron powder with a ball mill, graphitization, and removing iron from bio-graphite through a sulfuric acid wash.

To optimize the catalytic graphitization procedure, the effect of pre-heating carbonization temperature, iron catalyst loading, and graphitization temperature on graphite quality and crystallite size were systematically investigated, as illustrated in **Figure 2a–c**. The improvement in graphite crystallite size is crucial for maximum conductivity in bio-graphene inks as discussed further below.

Pre-heating biomass under inert atmosphere leads to the production of bio-oils and gases during the conversion of biomass to biochar.[17,20] Thus the initial set of studies focused on the exploring the effect of this preheating step. The hardwood samples were carbonized with a pre-heating step at temperatures ranging from 700 to 1200 °C, and the resulting biochar was further graphitized to investigate the impact of different pre-heating carbonization temperatures on the graphite crystallite size (Figure 2a). Graphitization conditions had an iron catalyst loading and graphitization temperature of 200 m_C% and 1200 °C respectively. After the graphitization, X-ray diffraction (XRD) was used to characterize the resulting material. XRD patterns of graphite generally show a peak at ≈26.2° (002) and a peak at ≈42.2° (100). The (002) peak corresponds to diffraction in the c-direction perpendicular to graphene plane, and the (100) peak corresponds to diffraction

S. J. Rowan
Chemical and Engineering Sciences
Argonne National Laboratory
9700 S Cass Ave, Lemont, IL 60439, USA

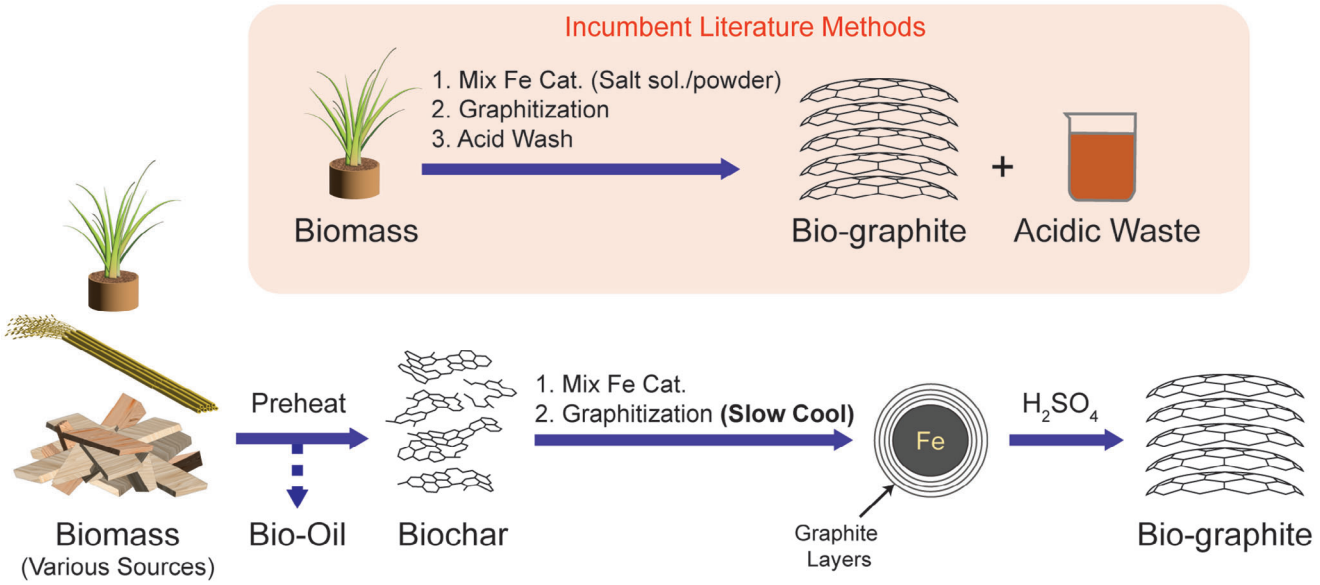

Figure 1. Bio-graphite production in literature compared to an overview of this bio-graphite production method. (The dashed arrows are out of the scope of this paper.)

in the a-direction, which is parallel to the direction of graphene plane. With the XRD data, the crystallite size can be calculated based on the Scherrer equation (Equation 1):

$$L = \frac{K\lambda}{B(2\theta)\cos(\theta)} \quad (1)$$

where L is the mean size of the crystalline domains, K is a dimensionless shape factor, λ is the X-ray wavelength, $B(2\theta)$ is the corrected full width at half maximum (FWHM) of the related peak, and θ is the Bragg angle.[21,22] When the (002) peak is used in the Scherrer equation, the L is L_c, and the L_a is instead calculated with the (100) peak.

While the L_c of the bio-graphite exhibited minimal change with increasing pre-heating carbonization temperature, L_a did show an enhancement. This observation is consistent with the higher pre-heating carbonization temperature increasing the percentage of carbon in the biochar,[23] which will reduce the number of defects during catalytic graphitization. It was also found that the pre-heating carbonization step had the added benefit of weakening the biomass structure, facilitating more homogeneous biochar-iron mixing. The pre-heating carbonization temperature of 1100 °C was selected as the optimal temperature due to the higher L_a observed in the bio-graphite compared to samples pre-heated at lower temperatures. Further elevating the pre-heating carbonization temperature did not yield any significant improvement in the quality of the bio-graphite and increases the energy consumption required for the processing.

The trends of L_c and L_a for bio-graphite prepared with different mass percentages of iron catalyst relative to biochar are shown in Figure 2b (preheat temperature 1100 °C, graphitization temperature 1200 °C). At higher iron loadings a significant increase in L_a and a minor increase in L_c is observed. This observation aligns with findings and hypotheses from previous studies – higher iron loading raises the possibility of fusion between catalyst droplets, and subsequently provides a flatter droplet surface that increases the average size of graphitic domains through a dissolution-precipitation mechanism, ultimately resulting in graphite crystals with fewer defects.[13,14] It is anticipated that further increases of iron loading may also improve bio-graphite crystallinity. However, increasing iron loading beyond 200 m_C% can compromise the environmental friendliness of the bio-graphite production because of the processing required to recover the iron catalyst. Thus, an iron loading of 200 m_C% was chosen to balance enhanced crystallinity with the required amount of iron powder per batch.

The final study was to explore the impact of the graphitization temperature (1000-1250 °C). Figure 2c displays the crystallite sizes of the bio-graphite prepared at various graphitization temperatures. According to the Fe-C phase diagram, the eutectic temperature of austenite is ≈1148 °C, which is the lowest possible melting temperature for Fe-C alloys.[24] The heating of the Fe-C mixture beyond that temperature can lead to accelerated graphitization by inducing a liquid phase. It was found that L_c and L_a increase with rising graphitization temperature, reaching their peak at 1200 °C. Further elevation of the graphitization temperature did not significantly impact graphite quality. Therefore, 1200 °C was identified as the optimal graphitization temperature.

To characterize the formation of graphite on the iron catalyst, scanning electron microscopy (SEM) was performed on the iron catalyst, hardwood char, and spherical particles after graphitization but before the acid treatment (Figure 2d–f). The spherical particles after graphitization inherited the round shape of the iron-carbon melt. Figure 2g,h presents the energy-dispersive X-ray spectroscopy (EDS) carbon and iron distribution maps of Figure 2f, respectively. After acid treatment, the iron core is removed, leaving a hollow spherical shell composed of a layered graphite structure (Figure 2i). These images reveal that the carbon is distributed on the surface of the spherical shell, covering

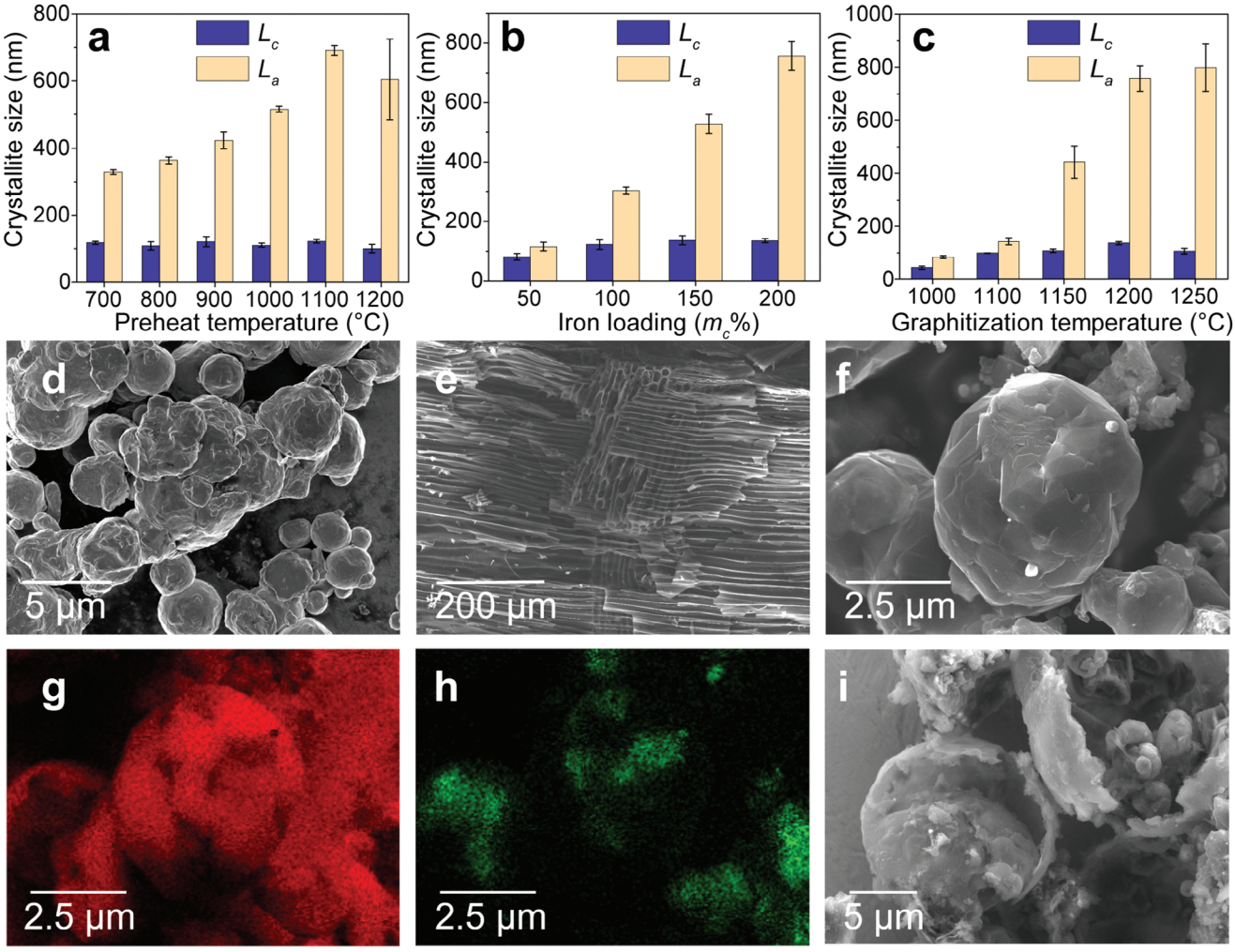

Figure 2. Optimization of bio-graphite production and characterization of iron and bio-graphite with and without acid wash. a) Graphite crystallite size in c-direction (L_c) and a-direction (L_a) of the bio-graphite product using different pre-heating carbonization temperatures ($n = 3$). Data are presented as mean ± SD of all samples analyzed in each group b) L_c and L_a of the bio-graphite product using different iron loadings ($n = 3$). Data are presented as mean ± SD of all samples analyzed in each group. c) L_c and L_a of the bio-graphite product using different graphitization temperatures ($n = 3$). Data are presented as mean ± SD of all samples analyzed in each group. The scanning electron microscopy (SEM) images of (d) iron catalyst, e) hardwood biochar, and f) bio-graphite without iron removal, and the corresponding g) carbon and h) iron distribution in energy-dispersive X-ray spectral mapping. i) SEM image of hardwood-derived bio-graphite.

most of the area, while the iron is primarily distributed inside the particle.

The iron powder catalyst has an average size of 2 µm, as shown in Figure 2d. However, after catalytic graphitization and acid washing, the spherical graphite shells have an average size of around 10 µm (Figure 2i). This observation is consistent with previous studies where the smaller iron particles fusing at 1200 °C aid the growth of larger graphite layers.[13,14] X-ray photoelectron spectroscopy (XPS) of the obtained bio-graphite (Figure S1a-b, Supporting Information) and natural graphite (Figure S2a-b, Supporting Information) was undertaken to further evaluate the surface element distribution and electronic structure of carbon. Based on XPS, bio-graphite has a large carbon peak, which is predominantly sp^2 hybridized with small amount of sp^3 hybridized carbon. The O, Si, and Cl peaks of bio-graphite as impurities (Figure S1a, Supporting Information) are notably smaller than those observed in commercial natural graphite (Figure S2a, Supporting Information), underscoring the high purity of the synthesized bio-graphite.

To better compare this optimized protocol using a pre-heating carbonization step with literature protocols that directly use biomasses in graphitization,[13,18] bio-graphite was also prepared directly with hardwood powder. The usage of either iron salt or iron powder was also explored to investigate whether this choice changes overall bio-graphite quality prepared with hardwood powder.[13,18] To perfuse the iron salt homogenously, the ground hardwood powder was soaked in 1 M $FeCl_3$-IPA solution under vacuum as described in literature.[13] If iron powder was used as the catalyst, 200 $m_{hardwood}$% of iron powder was ball milled with the hardwood powder. After that, each sample was pyrolyzed directly at 1200 °C for graphitization. The Raman and XRD results of the bio-graphite obtained directly from the hardwood

(Biomass+Fe, Biomass+Fe Salt), along with the bio-graphite prepared from pre-heated biochar and iron powder (Biochar+Fe), are provided in Figure S3 (Supporting Information). With Raman spectroscopy, graphite typically exhibits a D peak at 1355 cm^{-1} related to the boundary of the graphite crystallites, and a G peak at 1575 cm^{-1} related to the graphite crystal structure.[25] The intensity ratio of D peak and G peak (I_D/I_G) is inversely proportional to the graphite crystallite size in the a-direction (L_a) of the graphite.[25,26] Bio-graphite prepared with pre-heating carbonization biochar exhibits the lowest I_D/I_G and highest L_c and L_a. These results emphasize that the pre-heating carbonization of biochar is essential and can lead to higher crystallinity of graphite without changing the catalyst loading or graphitization temperature.

The cooling rate during the graphitization step is seldom discussed as an essential variable to improving graphite quality. However, slower cooling is well-known to aid crystal growth and in a 1967 paper, Austerman et al. grew graphite single crystal from graphite-iron solution at a cooling speed of 20-60 °C per day.[27] Inspired by this logic, a series of slow cooling experiments were designed to explore the optimal graphitization conditions for bio-graphite preparation. Four different cooling periods were tested for the cooling from 1200 °C to 1100 °C, namely 10min (standard), 4h, 8h, and 12h. The 1200 °C to 1100 °C range was chosen with reference to the eutectic temperature of austenite mentioned previously. SEM images of bio-graphite from these cooling regimes are shown in **Figure 3**a–h. The graphite shell exhibits a thinner, and more poly-crystalline structure with standard cooling within 10 min (Figure 3a,b), whereas increasing cooling time gives bio-graphite a thicker, flatter, and more uniform structure (Figure 3c–h). With 12 h slow cooling, some bio-graphite even exhibits a single-crystal-like hexagonal shape. In addition to the micron-scale graphitic features, the nanoscale stacking also benefits from slow cooling. TEM shows that the 4h slow cool bio-graphite (Figure 3j) exhibits a clearer lamellar stacking structure in the (002) direction, indicative of a more uniform graphitic structure compared to the 10min cooling counterpart (Figure 3i). BET tests show that bio-graphite with longer slow cooling has less surface area, which indicates a structure with fewer defects (Figure S5, Supporting Information). Moreover, asymmetry of the Raman 2D peak located at ≈2700 cm^{-1} only occurs in samples with slow cooling (Figure 3k). This indicates that the slow-cooled bio-graphite has improved alignment in the c-direction stacking, matching the profile observed for natural graphite.[28] Slow cooling also leads to a graphite structure with fewer defects based on a comparison of metrics from Raman spectra. The I_D/I_G ratio of increasingly slow-cooled bio-graphite, and the corresponding L_a calculated from that ratio are shown in Figure 3l. Slow cooling up to 12 h reduces the I_D/I_G ratio from 0.25 to 0.06 and increases L_a from 76 to 310 nm, which more uniform graphite growth and larger crystallite size in the a-direction.

Figure 3m,n shows the Raman and XRD spectra of bio-graphite derived from hardwood synthesized with the optimized conditions (pre-heating carbonization temperature = 1100 °C, iron loading = 200 m_C%, graphitization temperature = 1200 °C, and slow cooling time = 12 h), alongside commercial natural graphite. According to the Raman spectra (Figure 3m), the bio-graphite derived from hardwood exhibits a similar I_D/I_G to the commercial natural graphite (I_D/I_G = 0.051 and 0.050 respectively). Calculated from the XRD spectra (Figure 3n), the hardwood bio-graphite has a graphite crystallite size of L_c = 285 ± 8 nm and L_a = 2.08 ± 0.14 µm, which are larger than the size of commercial spheroidized natural graphite (L_c = 177 ± 4 nm and L_a = 1.06 ± 0.06 µm). Thus, both Raman and XRD measurements indicate that a high-quality graphitic crystalline structure has been formed from the optimized graphitization process, yielding comparable or better results than commercial graphite products.

To explore if this graphitization process could be applied to other biomass, a range of biomass crops such as switchgrass (*Panicum virgatum*), cotton (*Gossypium spp.*), hemp (*Cannabis sativa*), miscanthus (*Miscanthus x giganteus*) and corn stover were also investigated. All biomass types were successfully graphitized using the optimized process and exhibited a sharp (002) peak representative of graphite growth (see Figure S4, Supporting Information for XRD and Raman spectra).

2.2. Life-Cycle Assessment of Bio-Graphite Production

The life-cycle energy consumption and greenhouse gas (GHG) emissions of the bio-graphite produced with this protocol were evaluated based on ISO 14040/44 standards.[29,30] These results were directly compared against LCA results for bio-graphite produced with other methods,[17,18,31,32] and against baseline synthetic and natural graphite values (**Figure 4**a; Tables S1 and S2, Supporting Information).[33] In carrying out this LCA, a functional unit of one metric ton of graphite was used with the system boundary depicted in Figure 4b. Bio-graphite produced with this method exhibits a 16% and 28% reduction in fossil fuel demand compared to the extraction of spheroidized natural graphite and the production of synthetic graphite, respectively.[33] Similarly, GHG emissions for this bio-graphite are markedly lower (44%, 47%) than spheroidized natural graphite and synthetic graphite.

Several characteristics of this synthetic protocol underpin these reductions in environmental impact. First, the pre-heated carbonized biochar feedstock has a high carbon content, can remove CO_2 by sequestering carbon in bio-graphite, and can be produced from various local biomasses or sourced as a co-product from industrial cellulosic renewable diesel processes.[34,35] Second, the higher carbon content starting material from this procedure enables a 69% yield, much larger than other reported methods, which only achieve 37% yield from pure lignin[31] and 18% yield from hardwood.[18] In addition, sulfuric acid is used to remove iron, as it allows recovery of the iron with electroplating to lower the material consumption (Figure S6, Supporting Information), while limiting the production of toxic gases. Overall, the LCA results clarify the environmental advantages of this bio-graphite synthesis method.

2.3. Fabrication and Performance of Bio-Graphite Derived Graphene Inks

Top-down production of graphene from sustainable biomass-related materials has long been of interest, but has previously been limited to producing highly oxidized, porous, defective, or low-conductivity (≤10^3 S m^{-1}) graphene-like materials. The

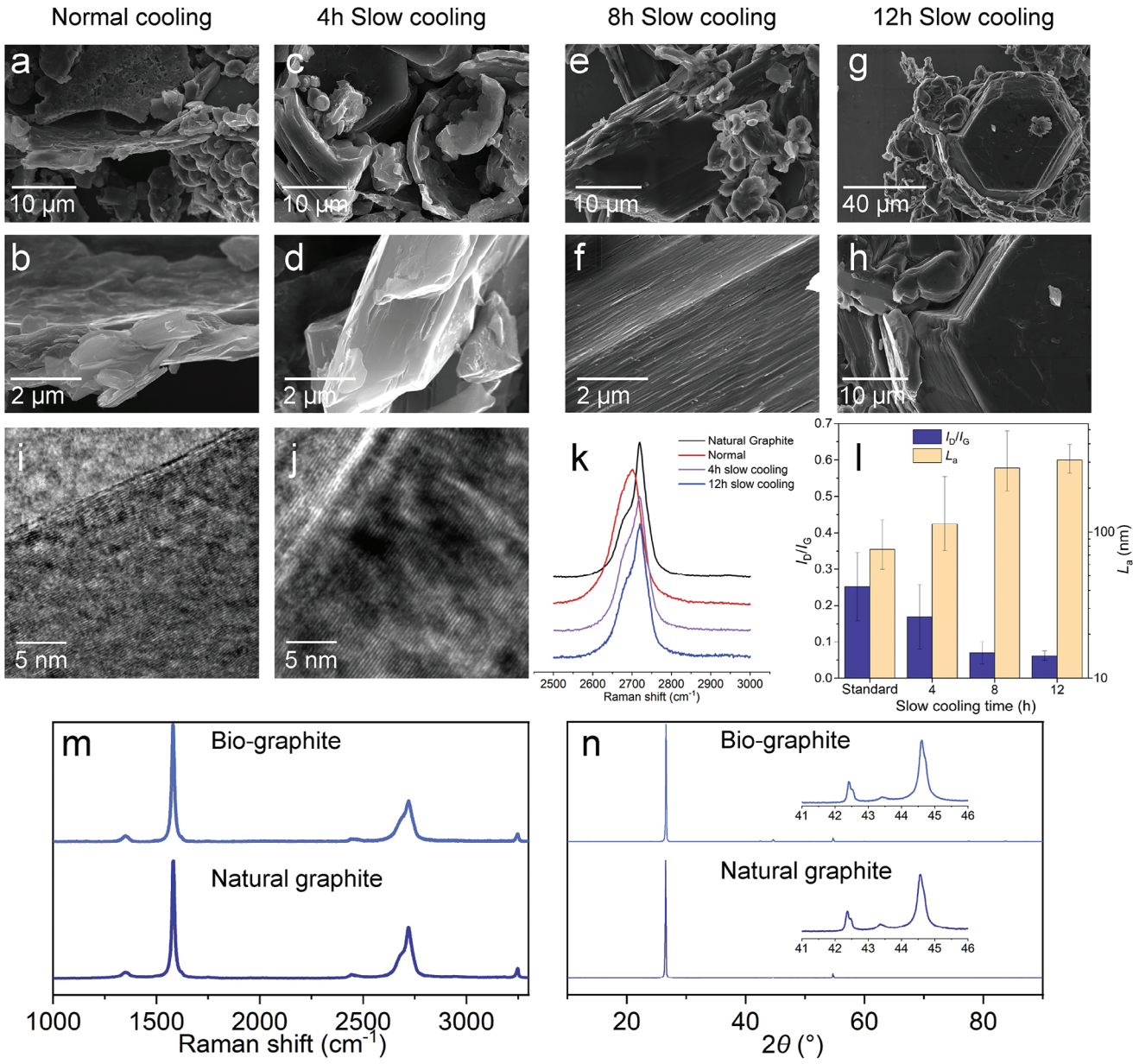

Figure 3. Influence of slow-cooling on bio-graphite production. SEM images of a,b) standard cooling bio-graphite, c,d) 4h slow cooling bio-graphite, e,f) 8h slow cooling bio-graphite, and g,h) 12h slow cooling bio-graphite; Transmission electron microscopy (TEM) images of (i) 10 min (standard) cool bio-graphite and j) 4h slow cool bio-graphite; k) Raman 2D peak of natural graphite, normal bio-graphite, and slow cool bio-graphite; l) I_D/I_G from Raman ($n = 4$, and data are presented as mean ± SD of all samples analyzed in each group) and corresponding L_a of hardwood derived bio-graphite prepared with different methods; (m) Raman spectra of 12h slow cool bio-graphite and commercial natural graphite, (n) XRD patterns of 12h slow cool bio-graphite and commercial spheroidized natural graphite.

preparation methods of carbon materials and the electrical conductivity of the biomass-derived films in previous studies are summarized in Table S3 (Supporting Information). The highly graphitic structure obtained from the slow-cooled hardwood bio-graphite product was encouraging toward large-scale, high-quality graphene production using liquid phase exfoliation (LPE). As such, the bio-graphite was used as a direct replacement for natural graphite flakes in a previously developed scalable LPE scheme using ethyl cellulose (EC) and ethanol.[36,37] EC acts as a dispersant or steric stabilizer to assist the shear exfoliation of the bio-graphite using ultrasonication, allowing for the stable formation of graphene nanoplatelets in ethanol solution. The exfoliated dispersion was then centrifuged and flocculated to form a bio-graphene composite powder that can be reformulated into different printable inks (see Experimental section in SI). The overall yield of the procedure was 4.6% conversion from graphite to graphene/EC powder or 0.9% conversion to pure graphene powder as adjusted by thermal gravimetric analysis (Figure S7a, Supporting Information), which is comparable to LPE on standard graphite raw materials previously reported

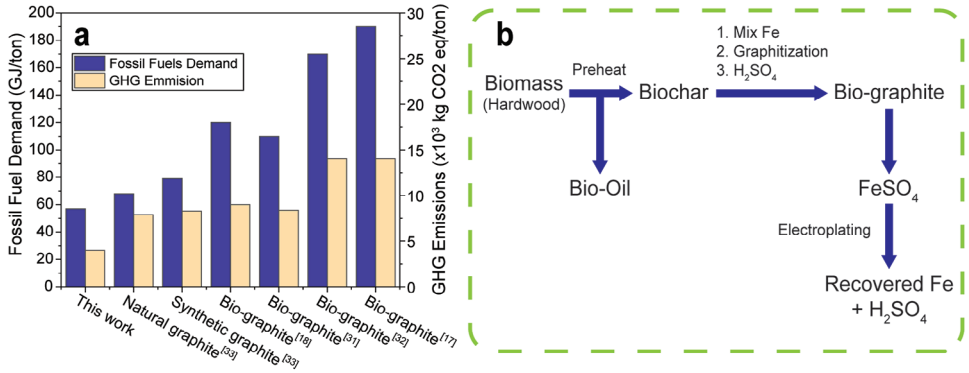

Figure 4. LCA results. a) Life-cycle fossil fuel consumption (GJ) and greenhouse gas emissions ($\times 10^3$ kg CO_2e) per metric ton graphite for different synthesis methods. b) System boundary for our bio-graphite synthesis method.

in the literature.[36] The production of graphene nanoplatelets was then confirmed via AFM measurements and changes in the Raman and XRD profiles (**Figure 5**; Figure S7, Supporting Information). Specifically, the average lateral size and thickness of the bio-graphene as measured by AFM was 192.4 nm and 4.1 nm respectively, indicating the generation of graphene-like nanoplatelets (Figure 5a,b). The increased intensity of the Raman D peak and more symmetric 2D peak after exfoliation both indicate changes in the defect structure between bio-graphite and bio-graphene (Figure S7b, Supporting Information). In particular, the increase in the D peak can be attributed to the edge-defects from shearing into flakes, and the loss of the 2D peak shoulder is indicative of the exfoliation yielding graphene structures that contain a few layers.[38] XPS measurements and fitting for the exfoliated graphene powder also show minimal oxidation and a substantial sp^2 C = C band after exfoliation that supports the formation of graphene-like material (Figure S7c, Supporting Information). Changes in XRD further indicate the exfoliation of the bulk crystal into a thin graphene-like structure based on the broadening and decreased intensity of (002) and (100) peaks that suggest the loss of crystallinity in the c-direction (Figure S7d, Supporting Information).[39] High-resolution transmission electron microscopy (HRTEM) images from drop cast bio-graphene solutions also depicts the formation of few-layer graphene nanoplatelets and shows the atomic layers of carbon visible in the folding edges, as well as the typical six-fold rotationally symmetric hexagonal structure in the planar lattice (Figure 5c,d). In particular, the inner peaks of the fast Fourier transform (FFT) shown in the Figure 5d inset have higher intensity than the outer ones, supporting that the highlighted blue region is indeed monolayer graphene. More detailed TEM images on regions with few-layer graphene can be found in the Supporting Information (Figure S8, Supporting Information). Overall, characterization of the exfoliated bio-graphite supports the formation of graphene-like materials as a higher-value product for use in printable electronics.

To confirm the electrical characteristics, the bio-graphene powder was formulated into a spin-coating ink and a screen-printable ink. Spin-coating was used for rapid testing of graphene conductivity, whereas screen printing was shown as a scalable technique that allows for roll-to-roll processing of high-resolution features for electronic devices. SEM of the cross-section and top-down view of the printed films indicate uniform stacking of flakes to create a percolating network (Figure 5e,f). The spin-coated films achieved a conductivity of 3.58×10^4 S m^{-1}, and the screen-printed bio-graphene films reached a conductivity of 2.35×10^4 S m^{-1}. The high conductivity of both types of films as observed in charge transport and profilometry measurements demonstrates the versatility of the bio-graphene to be deposited in multiple methods depending on the required application (Figure 5g). Notably, both graphene films achieved conductivities significantly higher than state-of-the-art biomass-based graphene-like materials (Figure 5h).[40,41] This impressive conductivity is enabled by the higher quality bio-graphite used for exfoliation, as suggested by the correlation between the L_a of the bio-graphite and the conductivity of the exfoliated bio-graphene film (Figure S7e, Supporting Information). It is also worth mentioning that the exfoliated graphene yield was highest for the 4h slow cool bio-graphite and was the condition used for all characterization and printing. Although the 12h slow cool bio-graphite achieved the highest crystallinity values, it was hypothesized that the thicker graphitic shell formed can cause more difficulty in intercalation during exfoliation, decreasing yield and only marginally improving graphene conductivity (Figure S7f, Supporting Information). By solely using benign additives in the exfoliation of the biomass-based graphene, this method is an avenue for the sustainable manufacturing of printable electronics components.

3. Conclusion

In conclusion, this study provides an innovative and sustainable method for producing high-quality bio-graphite from biochar, which is a renewable material stream from the cellulosic renewable diesel industry. The bio-graphite product was found to have crystallite sizes and spectroscopic quality metrics equal to or exceeding that of commercial spheroidized natural graphite. Furthermore, the bio-graphite was directly used to create bio-graphene nanoplatelets, enabling the scalable production of spin-coatable and screen-printable graphene inks for electronic device components. These conductive inks demonstrated conductivity values as high as 3.58×10^4 S m^{-1}, which is comparable to those derived from natural graphite, marking it the highest conductivity film achieved with fully biomass-derived graphene materials. By utilizing agricultural residues and biomass crops to create

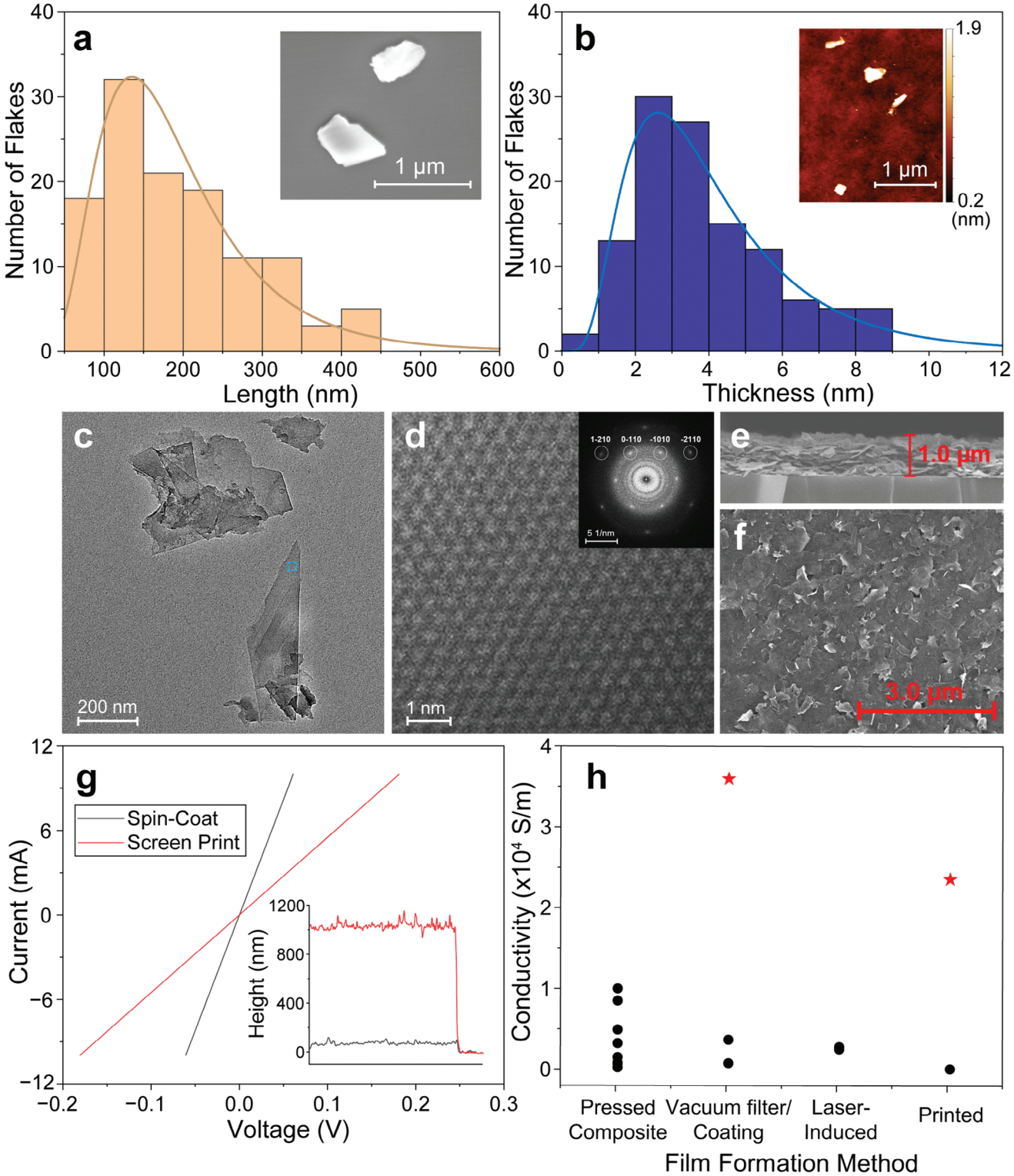

Figure 5. Bio-graphene characterization and printing performance. a) Atomic force microscopy (AFM) histograms for measured lateral length of bio-graphene flakes (n = 120 flakes). with representative SEM image of flakes inset, b) Atomic force microscopy (AFM) histograms for measured thickness of bio-graphene flakes (n = 120 flakes). with representative AFM image of flakes inset, c) Top-down TEM image of exfoliated bio-graphene flakes on an ultrathin lacey carbon coated grid. d) Atomic-resolution HRTEM image of the blue-squared region in (c), visualizing the hexagonal in-plane lattice structure of monolayer graphene. The inset is an FFT of the region, displaying the typical sixfold symmetry of monolayer graphene. e) Cross-sectional and f) top-down SEM images of screen-printed bio-graphene films, g) Current-voltage curves and profilometry scans (inset) for spin-coated and screen-printed bio-graphene films, h) Literature comparison of conductivity of films and composites made from solely biomass graphene materials. Red stars depict the conductivity achieved in this work.

biochar, this approach offers the promise of local graphite production with reduced emissions as confirmed by LCA. Overall, this work highlights the potential of bio-graphite synthesis as a more sustainable, energy-efficient, and low-emission alternative to traditional graphite production methods, heralding a promising future for biomass waste utilization.

4. Experimental Section

Materials: The two types of commercial natural graphite used as references were obtained from Sigma Aldrich. Natural graphite flake (808091) was used for the reference of Raman and XPS data. Graphite anode powder (advanced natural graphite, 907154) was used for XRD reference. Ethanol (Decon Labs, 200 proof) was purchased from Fisher Scientific. Ethyl cellulose (4cP), concentrated sulfuric acid, and the iron powder (<10 µm) were from Sigma Aldrich. Hardwood chips from yard trimmings and pyrolyzed hardwood char (preheated at 1100 °C, N_2 protected) were generously provided by American GreenFuels Rockwood (Tennessee), LLC, a wholly owned subsidiary of Kolmar Americas, Inc. Hardwood chips and pyrolyzed hardwood char were the input and byproduct, respectively, from their cellulosic renewable diesel production process. Cotton-based cellulose is filter paper from Fisher Scientific. The switchgrass, hemp, and miscanthus (MxG) grown as bioenergy feedstocks were harvested from the University of Illinois Energy Farm.

Pre-Heating Carbonization Step: Biomasses were heated to various temperatures (700-1200 °C) and held for 1 h to yield a preheated carbonized material.

An Example of Biochar Prepared with Hardwood at 1100 °C: Hardwood chips of ≈2 cm diameter were placed directly into a tube furnace (MTI cooperation, OTF-1500X-UL-3) and heated to 1100 °C at a rate of 10 °C min^{-1} under nitrogen protection (flow rate = 150-200 sccm), maintained at 1100 °C for 1h, cooled to 600 °C at a rate of 10 °C min^{-1}, and then naturally cooled to room temperature.

Graphitization and Acid Washing Step: Biochar as described above was used directly in a second stage of pyrolysis with higher temperatures for graphitization. If not specified, the biochar was the preheated carbonized hardwood char as received from Kolmar (heated within their processing up to 1100 °C), the iron loading is 200 m_C%, and the graphitization temperature is 1200 °C.

An Example of Bio-Graphite Prepared with Hardwood Biochar and 200 mC% Iron Powder at 1200 °C: 30.0 g Biochar and 60.0 g iron powder were added to the ball mill (Tencan powder technology, QM-5). The ball mill was set at a rate of 120 rpm and run for 3 h. The resulting powder was passed through a 100 Mesh sieve and placed in a tube furnace. Nitrogen gas was flowed through the tube (100-200 sccm), before the furnace was heated to 1200 °C at a rate of 10 °C min^{-1}, maintained at a constant temperature for 1 h, cooled to 600 °C at a rate of 10 °C min^{-1}, and then naturally cooled to room temperature. 70 mL of concentrated sulfuric acid, 500 mL of deionized water, and 50 mL of ethanol were added to a beaker and mixed well. Then, the powder obtained from graphitization was slowly added to the beaker under magnetic stirring, and the mixture was allowed to stir overnight at room temperature. Bio-graphite was extracted by filtration of the mixture followed by washing with deionized water until the pH of the filtrate was above 6. The black powder was dried with air flow for 3 days to obtain bio-graphite as the final product. To obtain an accurate yield bio-graphite powder was further vacuum oven dried at 120 °C overnight, resulting in 20.7 g (69%).

Slow Cooling: After the biochar and iron powder mixture were maintained at 1200 °C for an hour, the slow cooling was done by linearly reducing temperature from 1200 to 1100 °C over the specific time. After that, the mixture was cooled to 600 °C at a rate of 10 °C min^{-1}, and then naturally cooled to room temperature.

Bio-Graphite Prepared with Similar Procedures in the Literature: *Biomass and Iron Salt*: 1.73 g of oven-dried hardwood powder (diameter less than 1 mm) was soaked in 100 mL 1 M $FeCl_3$-IPA solution under vacuum overnight.[13] The wood was then filtered and oven-dried to yield 1.90 g of Fe-impregnated hardwood. The resulting powder was placed in a tube furnace. Nitrogen gas was flowed through the tube (100-200 sccm), before the furnace was heated to 1200 °C at a rate of 10 °C min^{-1}, maintained at a constant temperature for 1 h, cooled to 600 °C at a rate of 10°C min^{-1}, and then naturally cooled to room temperature. The resulting powder was washed with 1 M sulfuric acid followed by DI water until neutral, and finally vacuum oven-dried at 120 °C overnight to produce 0.66 g of bio-graphite (38% yield).

Biomass and Iron: 0.87 g of oven-dried hardwood powder (diameter less than 1 mm) and 1.74 g of iron powder were mixed by milling.[18] The resulting powder was placed in a tube furnace. Nitrogen gas was flowed through the tube (100-200 sccm), before the furnace was heated to 1200 °C at a rate of 10 °C min^{-1}, maintained at a constant temperature for 1 h, cooled to 600 °C at a rate of 10 °C min^{-1}, and then naturally cooled to room temperature. The resulting powder was washed with 1 M sulfuric acid followed by DI water until neutral, and finally vacuum oven-dried at 120 °C overnight to produce 0.24 g of bio-graphite (28% yield).

Raman Spectroscopy: Raman spectroscopy was conducted on a Horiba LabRAM HR Evolution system with a 532 nm excitation laser.

X-Ray Diffraction: The X-ray diffraction (XRD) of bio-graphite was conducted on a Bruker D8 Powder X-ray Diffractometer. The measurement of the crystallite sizes is based on a literature method.[22] The samples were prepared by dispersing bio-graphite powder in acetone and drop casting on a silicon zero diffraction plate to form a thin film (less than 0.1 mm). The conditions for coarse testing were a scan width of 0.01°, scan speed of 10° min^{-1}, and scan range of 5°-90°. The conditions for fine testing were a scan width of 0.0025° and scan speed of 1° min^{-1} over the scan range of interest. The XRD results of bio-graphite were corrected with the data of Si powder as external standard, which was purchased from Sigma-Aldrich.

Scanning Electron Microscopy and Energy Dispersive X-Ray Spectroscopy: Scanning electron microscopy (SEM) was conducted using a Carl Zeiss Merlin High-Resolution Field Emission Scanning Electron Microscope (FE-SEM). The SEM was operated under the SE2 or InLens mode. The samples were placed on copper tape stuck onto stubs. The samples were tested without further coating. Energy dispersive X-ray spectroscopy (EDS) was performed on a Carl Zeiss Merlin High-Resolution FE-SEM coupled with an Oxford Ultim Max 100 EDS System.

Transmission Electron Microscopy: Transmission electron microscopy (TEM) images were obtained using a 300KV FEI Tecnai F30 Microscope. Samples for TEM were prepared by depositing one droplet of diluted bio-graphite suspension in toluene onto a lacey carbon grid from Ted Pella.

X-Ray Photoelectron Spectroscopy: X-ray photoelectron spectroscopy (XPS) for bio-graphite was conducted using a Kratos AXIS Nova System that uses a monochomatic Al Kα X-ray source with a delay line detector (DLD) system. The samples were prepared by dispersing the bio-graphite powder in acetone and drop casting on a silicon plate. The carbon region data were analyzed based on methods in the literature[42] with CasaXPS software. For bio-graphene, XPS measurements were conducted using an ESCALAB 250Xi spectrometer (Thermo Fisher Scientific) with an Al Kα radiation source using a laser spot size of 500 µm. The resulting spectra were charge-shifted and fitted using Thermo Avantage software.

Electroplating: The electrodeposition of iron was performed on an interface 1010E potentiostat from Gamry Instruments. All tests were performed using a standard 2-electrode electrochemical cell. Pt wire electrode (CH Instruments CHI115) was selected as the counter electrode. To simulate purified wastewater after acid wash, one drop of concentrated H_2SO_4 was added into 1 M $FeSO_4$ solution. Copper wire was selected as the working electrode and weighed before deposition. The electroplating of Fe was carried out by holding the current constant at 100 mA for 5 min. The electrodes were then dried and weighed again. The weight difference before and after the deposition was taken as the deposited Fe amount (m_{Fe}), which was determined to be 16.04 mg. Faradaic efficiency (FE) was calculated to be 92% using Equation 2:

$$FE = \frac{\frac{m_{Fe}}{M_{Fe}} F}{It} \quad (2)$$

where M_{Fe} is the molecular weight or iron, F is the faradaic constant (96485 C mol^{-1}), I is the deposition current, and t is the deposition time. Figure S5 (Supporting Information) shows the recorded voltage plotted with time during the electroplating at a constant current $I = 100$ mA.

Bio-Graphene Exfoliation: Bio-graphene exfoliation and ink formulation were adapted from a previously described scalable liquid-phase exfoliation procedure.[5] Briefly, the bio-graphite was first dispersed in a solution of ethyl cellulose (EC) in ethanol (50 mg mL^{-1} bio-graphite, 10 mg mL^{-1} EC) and horn sonicated at high speed (10 300 rpm) for 10 h in a VCX750 horn sonicator. The unexfoliated and remaining graphitic material was removed by centrifugation at 4500 rpm (≈3,700 g) for 30 min (Avanti J26-XPI centrifuge, JS 7.5 rotor, Beckman Coulter). The supernatant containing exfoliated graphene nanosheets was flocculated with an aqueous sodium chloride solution (16:9 ratio of graphene dispersion:NaCl solution), which was further centrifuged at 7000 rpm (12 227 g) for 7 min to sediment out bio-graphene/EC flocs. The solid floc was washed thoroughly with deionized water using vacuum filtration and dried with an infrared lamp to obtain the final exfoliated bio-graphene/EC composite powder. This powder was determined to be 15.2% graphene-like material based on thermogravimetric analysis (Figure S7d, Supporting Information).

Bio-Graphene Ink Formulation and Printing: Screen printable bio-graphene inks were formulated with 150 mg mL^{-1} of bio-graphene/EC composite powder mixed in terpineol using a centrifugal mixer (Thinky USA, ARE-310) with 5 mm yttria-stabilized zirconia ball bearings for 60 min at increasing speeds from 500-2000 rpm. An automated screen printer (Hary Manufacturing Inc., 886PC DSIV) was used to rapidly pattern films onto polyimide or glass substrates with a custom-made screen design. The spin-coating ink used 40 mg mL^{-1} bio-graphene/EC powder in an ethanol and ethyl lactate (9:1 ratio) solution, which was sonicated overnight for homogeneity. Si/SiO_2 substrates were pre-cleaned with sonication in ethanol/isopropanol for 5 min each, and plasma cleaned to enhance graphene attachment before spin-coating into a uniform film. All films were annealed in a box furnace at 350 °C for 30 min after printing to remove excess cellulosic binder.

Bio-Graphene Characterization: The morphology of spin-coated or screen-printed films was characterized with scanning electron microscopy using a Hitachi SU8030 FEG SEM. An accelerating voltage of 5.0 kV was used for conductive samples. Charge-sensitive cross-sections of films were coated with 9 nm of osmium prior to scanning, and an accelerating voltage of 2.0 kV was used. A working distance of ≈8 mm was used for all SEM measurements. HRTEM samples were prepared by drop-casting the solution onto a 300-mesh 50-µm Cu grid with a continuous layer of ultrathin lacey carbon film (Electron Microscopy Sciences). HRTEM images were collected on aberration-corrected JEOL ARM200CF S/TEM operating at 200kV. Data was collected and processed using the Gatan Microscopy Suite (GMS) software.

Life Cycle Assessment: The life cycle assessment (LCA) conducted in this work is based on ISO 14040/44 standards.[29,30] Life cycle inventory data (e.g., energy and material input consumption amounts per metric ton of graphite) were integrated for our synthesis method and for methods reported in the literature into the Greenhouse Gases, Regulated Emissions and Energy Efficiency in Technologies (GREET) model with default settings for the U.S. national electricity grid and natural gas system.[33] With this approach, all background systems were identical for each bio-graphite synthesis method with biomass as starting materials. Table S1 (Supporting Information) reports the life cycle inventories used for each bio-graphite synthesis method.

Supporting Information

Supporting Information is available from the Wiley Online Library or from the author.

Acknowledgements

H.Y. and J.H. contributed equally to this work. This work was primarily supported by the National Science Foundation MADE-PUBLIC Future Manufacturing Research Grant Program (NSF Award Number CMMI-2037026). This work made use of the shared facilities at the University of Chicago Materials Research Science and Engineering Center, supported by National Science Foundation under award number DMR-2011854. Parts of this work were carried out at the Soft Matter Characterization Facility of the University of Chicago. This work made use of public facilities in the Northwestern University NUANCE Center and the Jerome B. Cohen X-Ray Diffraction Facility, which has received support from the Soft and Hybrid Nanotechnology Experimental (ShyNE) Resource (NSF ECCS-2025633), the IIN, and the Northwestern MRSEC program (NSF DMR-2308691). This work also made use of the MatCI Facility supported by the MRSEC program of the National Science Foundation (DMR-1720139) at the Materials Research Center of Northwestern University. The authors thank Zirui Zhou at the University of Chicago for testing and discussions on TEM. J.H. gratefully acknowledges support from the Ryan Fellowship and the International Institute for Nanotechnology at Northwestern University.

Conflict of Interest

The authors declare no conflict of interest.

Data Availability Statement

The data that support the findings of this study are available from the corresponding author upon reasonable request.

Keywords

biomass-derived, graphene ink, graphite, printed electronics, sustainability

Received: August 3, 2024
Revised: October 6, 2024
Published online:

[1] D. D. L. Chung, *J. Mater. Sci.* **2002**, *37*, 1475.
[2] M. Wissler, *J. Power Sources* **2006**, *156*, 142.
[3] R. Mills, Graphite deficit starting this year, as demand for EV battery anode ingredient exceeds supply, https://www.mining.com/web/graphite-deficit-starting-this-year-as-demand-for-ev-battery-anode-ingredient-exceeds-supply/ (accessed: May 2024).
[4] K. Magill, A looming graphite shortage could snarl the EV battery supply chain, https://www.utilitydive.com/news/graphite-shortage-ev-electric-vehicles-supply-chain/628371/ (accessed: May 2024).
[5] U. S. Geological Survey, Notice of Final Determination on 2023 DOE Critical Materials List, https://www.energy.gov/sites/default/files/2023-07/preprint-frn-2023-critical-materials-list.pdf (accessed: May 2024).
[6] M. Grohol, C. Veeh, Study on the critical raw materials for the EU 2023, https://data.europa.eu/doi/10.2873/725585 (accessed: May 2024).
[7] The Australian Government, Critical Minerals Strategy 2023–2030, https://www.industry.gov.au/publications/critical-minerals-strategy-2023-2030 (accessed: May 2024).
[8] J. Zhang, C. Liang, J. B. Dunn, *Environ. Sci. Technol.* **2023**, *57*, 3402.
[9] E. Benson, T. Denamiel, China's New Graphite Restrictions, https://www.csis.org/analysis/chinas-new-graphite-restrictions (accessed: May 2024).
[10] T. W. House, Building resilient supply chains, revitalizing american manufacturing, and fostering broad-based growth, https://www.whitehouse.gov/wp-content/uploads/2021/06/100-day-supply-chain-review-report.pdf (accessed: May 2024).

[11] D. Surovtseva, E. Crossin, R. Pell, L. Stamford, *J. Ind. Ecol.* **2022**, *26*, 964.
[12] R. D. Hunter, J. Ramírez-Rico, Z. Schnepp, *J. Mater. Chem. A* **2022**, *10*, 4489.
[13] A. Gomez-Martin, Z. Schnepp, J. Ramirez-Rico, *Chem. Mater.* **2021**, *33*, 3087.
[14] A. C. Ghogia, L. M. Romero Millán, C. E. White, A. Nzihou, *ChemSusChem* **2023**, *16*, 202201864.
[15] Q. Yan, J. Li, X. Zhang, J. Zhang, Z. Cai, *J. Mater. Chem. A* **2019**, *7*, 13978.
[16] N. A. Banek, K. R. McKenzie, D. T. Abele, M. J. Wagner, *Sci. Rep.* **2022**, *12*, 8080.
[17] N. A. Banek, D. T. Abele, K. R. McKenzie, M. J. Wagner, *ACS Sustainable Chem. Eng.* **2018**, *6*, 13199.
[18] W. J. Sagues, J. Yang, N. Monroe, S.-D. Han, T. Vinzant, M. Yung, H. Jameel, M. Nimlos, S. Park, *Green Chem.* **2020**, *22*, 7093.
[19] F. Mori, M. Kubouchi, Y. Arao, *J. Mater. Sci.* **2018**, *53*, 12807.
[20] M. Jahirul, M. Rasul, A. Chowdhury, N. Ashwath, *Energies* **2012**, *5*, 4952.
[21] F. T. L. Muniz, M. A. R. Miranda, C. Morilla dos Santos, J. M. Sasaki, *Acta Crystallogr. A* **2016**, *72*, 385.
[22] N. Iwashita, C. R. Park, H. Fujimoto, M. Shiraishi, M. Inagaki, *Carbon* **2004**, *42*, 701.
[23] F. Ronsse, S. van Hecke, D. Dickinson, W. Prins, *GCB Bioenergy* **2013**, *5*, 104.
[24] J. Chipman, *Metall. Trans.* **1972**, *3*, 55.
[25] F. Tuinstra, J. L. Koenig, *J. Chem. Phys.* **1970**, *53*, 1126.
[26] L. G. Cançado, K. Takai, T. Enoki, M. Endo, Y. A. Kim, H. Mizusaki, A. Jorio, L. N. Coelho, R. Magalhães-Paniago, M. A. Pimenta, *Appl. Phys. Lett.* **2006**, *88*, 163106.
[27] S. B. Austerman, S. M. Myron, J. W. Wagner, *Carbon* **1967**, *5*, 549.
[28] K. R. Paton, K. Despotelis, N. Kumar, P. Turner, A. J. Pollard, *Beilstein J. Nanotechnol.* **2023**, *14*, 509.
[29] International Organization for Standardization, ISO 14044:2006 Environmental Management—Life Cycle Assessment—Requirements and Guidelines, https://www.iso.org/standard/38498.html (accessed: May 2024).
[30] International Organization for Standardization, ISO 14040:2006 Environmental Management—Life Cycle Assessment—Principles and Framework, https://www.iso.org/standard/37456.html (accessed: May 2024).
[31] Q. Yan, X. Zhang, J. Li, E. B. Hassan, C. Wang, J. Zhang, Z. Cai, *J. Mater. Sci.* **2018**, *53*, 8020.
[32] M. Demir, Z. Kahveci, B. Aksoy, N. K. R. Palapati, A. Subramanian, H. T. Cullinan, H. M. El-Kaderi, C. T. Harris, R. B. Gupta, *Ind. Eng. Chem. Res.* **2015**, *54*, 10731.
[33] Argonne National Laboratory, The Greenhouse Gases, Regulated Emissions, and Energy Use in Technologies (GREET) Model, https://www.energy.gov/eere/greet (accessed: Jan 2022).
[34] J. H. Windeatt, A. B. Ross, P. T. Williams, P. M. Forster, M. A. Nahil, S. Singh, *J. Environ. Manage.* **2014**, *146*, 189.
[35] J. Lehmann, A. Cowie, C. A. Masiello, C. Kammann, D. Woolf, J. E. Amonette, M. L. Cayuela, M. Camps-Arbestain, T. Whitman, *Nat. Geosci.* **2021**, *14*, 883.
[36] A. C. M. de Moraes, J. Obrzut, V. K. Sangwan, J. R. Downing, L. E. Chaney, D. K. Patel, R. E. Elmquist, M. C. Hersam, *J. Mater. Chem. C* **2020**, *8*, 15086.
[37] E. B. Secor, M. H. Dos Santos, S. G. Wallace, N. P. Bradshaw, M. C. Hersam, *The J. Phys. Chem. C* **2018**, *122*, 13745.
[38] K. R. Paton, E. Varrla, C. Backes, R. J. Smith, U. Khan, A. O'Neill, C. Boland, M. Lotya, O. M. Istrate, P. King, T. Higgins, S. Barwich, P. May, P. Puczkarski, I. Ahmed, M. Moebius, H. Pettersson, E. Long, J. Coelho, S. E. O'Brien, E. K. McGuire, B. M. Sanchez, G. S. Duesberg, N. McEvoy, T. J. Pennycook, C. Downing, A. Crossley, V. Nicolosi, J. N. Coleman, *Nat. Mater.* **2014**, *13*, 624.
[39] A. Kushwaha, M. K. Jangid, B. B. Bhatt, A. Mukhopadhyay, D. Gupta, *ACS Appl. Energy Mater.* **2021**, *4*, 7911.
[40] W.-X. Dong, Y.-F. Qu, X. Liu, L.-F. Chen, *FlatChem* **2023**, *37*, 100467.
[41] X. Kong, Y. Zhu, H. Lei, C. Wang, Y. Zhao, E. Huo, X. Lin, Q. Zhang, M. Qian, W. Mateo, R. Zou, Z. Fang, R. Ruan, *Chem. Eng. J.* **2020**, *399*, 125808.
[42] M. C. Biesinger, *Appl. Surf. Sci.* **2022**, *597*, 153681.